

Energy & Environmental Science

Accepted Manuscript



This article can be cited before page numbers have been issued, to do this please use: Z. Xiao, C. Bi, Y. Shao, Q. Dong, Q. Wang, Y. Yuan, C. Wang, Y. Gao and J. Huang, *Energy Environ. Sci.*, 2014, DOI: 10.1039/C4EE01138D.

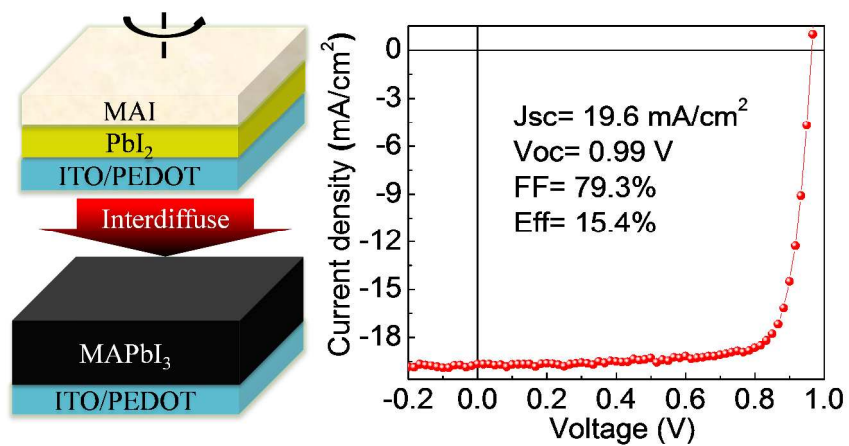


This is an *Accepted Manuscript*, which has been through the Royal Society of Chemistry peer review process and has been accepted for publication.

Accepted Manuscripts are published online shortly after acceptance, before technical editing, formatting and proof reading. Using this free service, authors can make their results available to the community, in citable form, before we publish the edited article. We will replace this *Accepted Manuscript* with the edited and formatted *Advance Article* as soon as it is available.

You can find more information about *Accepted Manuscripts* in the [Information for Authors](#).

Please note that technical editing may introduce minor changes to the text and/or graphics, which may alter content. The journal's standard [Terms & Conditions](#) and the [Ethical guidelines](#) still apply. In no event shall the Royal Society of Chemistry be held responsible for any errors or omissions in this *Accepted Manuscript* or any consequences arising from the use of any information it contains.



A new low-temperature all-solution approach was invented to produce perovskite solar cells with efficiency of 15.4% at high device yield.

COMMUNICATION

Efficient, High Yield Perovskite Photovoltaic Devices Grown by Interdiffusion of Solution-Processed Precursor Stacking Layers

Zhengguo Xiao,^{1†} Cheng Bi,^{1†} Yuchuan Shao,¹ Qingfeng Dong,¹ Qi Wang,¹ Yongbo Yuan,¹ Chenggong Wang,² Yongli Gao,^{2,3} and Jinsong Huang¹

Cite this: DOI: 10.1039/x0xx00000x

Received ooth ***** 2014,
Accepted ooth ***** 2014

DOI: 10.1039/x0xx00000x

www.rsc.org/

Abstract We report on an interdiffusion method to fabricate pin-hole free perovskite films using a low temperature (<105 °C) solution process. A high efficiency of 15.4%, with fill factors of ~80%, was achieved for the devices under one sun illumination. The interdiffusion method results in high device yield, with above 14.5% efficiency for more than 85% of the devices.

Organometal trihalide perovskites are emerging as a new generation of solution processable, low cost photovoltaic materials which are abundant in nature. High power conversion efficiency of around 15% has been achieved in both mesoporous structure devices as well as planar heterojunction (PHJ) devices.¹⁻¹⁷ In addition to the strong absorption in the ultraviolet visible range, organometal trihalide perovskites have intriguing optoelectronic properties, such as excellent crystallinity, very large carrier mobility comparable to silicon, bipolar transport, and large charge diffusion length which enables high performance devices with the traditional PHJ structure.^{2, 7, 12, 14-15, 17} In addition to the simple device structure, PHJ perovskite devices have been demonstrated to have better stability under ultraviolet (UV) light by removing mesoporous TiO₂, which causes instability due to the UV light-induced desorption of surface-adsorbed oxygen.¹⁸ Recent studies demonstrate that dual source vacuum sublimation technique produces homogeneous and densely packed perovskite film.^{2, 19} However, depositing a continuous, leakage-free perovskite film with a thickness comparable to the charge diffusion length using solution processes has proven to be very difficult.^{2, 7, 17, 20-21}

Noncontinuous perovskite films were frequently observed using lead iodine (PbI₂) and methylammonium halide (CH₃NH₃X, or MAX) blend, which might be related to the interaction of perovskite with a substrate surface.^{17, 20} Our recent observations indicate it may also be due to the low viscosity of the perovskite solution and the quick crystallization of the mixed precursor upon drying the spun films.²² The power conversion efficiency (*PCE*) of low-temperature solution-processed perovskite devices in the range of 4~12% were far below those devices with a mesoporous structure or fabricated by thermal evaporation.^{2, 4, 17}

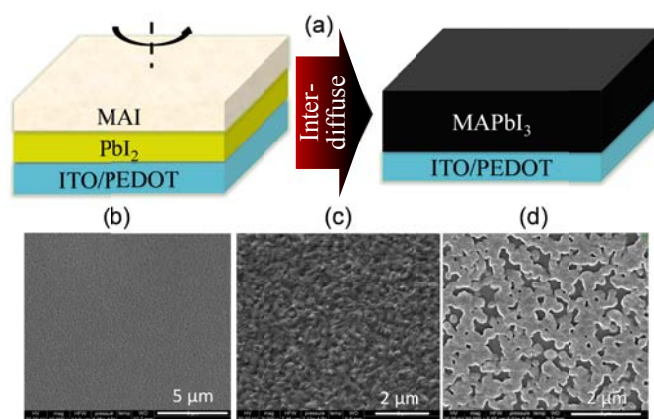


Fig. 1. (a) Schematics of spin coating of PbI₂ and MAI using orthogonal solvents and the conversion of the stacking layer into a perovskite layer upon annealing. (b-d) SEM image of the PbI₂ film (b), the annealed perovskite layer formed by an interdiffusion process (c), and the annealed perovskite film spun from the premixed PbI₂ and MAI solution (d).

In this manuscript, we report a method of forming continuous, compact iodine perovskite (MAPbI_3) films by the interdiffusion of spin-coated stacking layers of PbI_2 and MAI. The high quality film achieved allows the fabrication of leakage-free photovoltaic devices and a high *PCE* of 15.4% under one sun and 17.1% under 0.03 sun illumination.

The deposition and thermal annealing processes of the PbI_2 /MAI stacking layer films is illustrated in Fig. 1a. For the film fabrication, PbI_2 and MAI were first dissolved in dimethylformamide (DMF) and 2-propanol, respectively, as precursor solutions at varied concentration. The precursors were then spun onto poly(3,4-ethylenedioxythiophene) poly(styrenesulphonate) (PEDOT:PSS) covered indium tin oxide (ITO) glass with a PbI_2 layer underneath an MAI layer. A supersaturated hot solution of PbI_2 was used for quick drying to obtain a pin-hole free and conformal PbI_2 layer on the PEDOT:PSS surface. Since PbI_2 has relatively low solubility in 2-propanol, the spin coating of MAI did not wash off the PbI_2 . The bilayer films were then annealed at a temperature of 100 °C for varied durations. The SEM picture in Fig. 1b reveals a very continuous PbI_2 film, which is uncommon for an inorganic salt. The dried PbI_2 /MAI bilayer films are rougher than PbI_2 layers due to formation of MAPbI_3 microcrystals upon drying and thermal annealing. Nevertheless, they are still continuous and pinhole free across the whole device area, as shown by the large area SEM in Fig. 1c. More detailed procedures of the perovskite film fabrication can be found in supplementary information. In contrast, the MAPbI_3 films spun from premixed PbI_2 and MAI blend solutions generally are nonuniform with many microstructures on the surface, as shown in Fig. 1d.²²

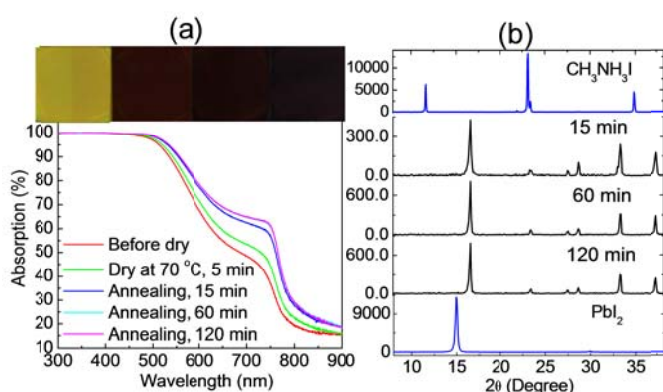


Fig. 2. (a) Single-path absorption of perovskite film after dry and various annealing durations. The inset shows the pictures, from left to right, of the spun PbI_2 film, the PbI_2 /MAI film before drying, the PbI_2 /MAI films after drying, and after 15 min. of annealing; (b)

XRD pattern of MAI, PbI_2 , and the perovskite films formed by interdiffusion with varied annealing times.

We studied the interdiffusion process of PbI_2 and MAI stacking layers. A thickness ratio of 1.4:1 for the MAI: PbI_2 layer, calculated from the density and molecular weight, is needed to form stoichiometry iodine perovskite by assuming a complete interdiffusion and reaction of the precursors. The thickness of the PbI_2 layer was varied from 40 nm to 200 nm, and the thickness of MAI varied from 60 nm to 250 nm by controlling the concentration of the precursor solutions and the spin rate, which are summarized in Table S1. There is a quick reaction of MAI and PbI_2 upon contact, evidenced by the immediate color change of the bilayer films observed right after the spin coating of the MAI layer, which is consistent with previous observations in mesoporous structure devices¹ Fig. 2a shows the evolution of the color change of the films at different stages.

The interdiffusion of the PbI_2 /MAI films and formation of perovskite after varied annealing times was studied by absorption spectra and X-ray diffraction (XRD). Fig. 2a shows typical absorption spectra of a PbI_2 /MAI stacking film after different annealing durations from 0 min. to 2 hr. at a temperature of 100 °C. The absorption at a wavelength of around 740 nm from the perovskite quickly increased during the first 15 min. of thermal annealing and then saturated after 1 hr. of annealing. The XRD patterns versus time of these films have the same variation trend with absorption spectra. As shown in Fig. 2b, both MAI and PbI_2 peaks disappear after 15 min. of annealing and remains almost unchanged afterwards. No impurity peaks were identified from XRD patterns. This indicates that the long-range interdiffusion of MAI and PbI_2 occurs primarily during the first 15 min. of annealing.

It should be noted that the interdiffusion approach reported here is very different from the sequential deposition method reported by *Burschka et al*¹ which makes good mesoporous structure perovskite solar cells but not PHJ ones. We dipped 140 nm PbI_2 film into MAI solution; however, we obtained very non-uniform, rough perovskite films, as shown in Fig. S1. The efficiency of the devices based on these films only reached 3.2%. The low performance can be explained by the difficulty of MAI to penetrate the thick PbI_2 films, crystallization caused very rough films. Another difference is that the thermal annealing process is required in the interdiffusion method reported here to make sure that the compact PbI_2 can be fully reacted

with MAI. In the mesoporous perovskite photovoltaic devices with porous TiO₂ structures,¹ PbI₂ absorbed on TiO₂ can be much thinner because of the very large surface area of mesoporous structure needed to absorb enough PbI₂. Due to the very thin PbI₂ in a mesoporous structure, the reaction of PbI₂ and MAI can be very quick and complete without resorting to thermal annealing. However, for the spun compact PbI₂ and MAI stacking layers, there is still unreacted MAI and PbI₂ right after deposition, shown by the SEM image of as-prepared PbI₂ and MAI stacking layers in Fig. S2. The devices made of such films show low *PCE*, below 1%, with typical S-shaped photocurrent, a signature of large series resistance caused by the insulating MAI and/or PbI₂. A thermal annealing is thus still needed to drive the interdiffusion of MAI and PbI₂, which can be visually observed by the increased darkness of the MAPbI₃ films.

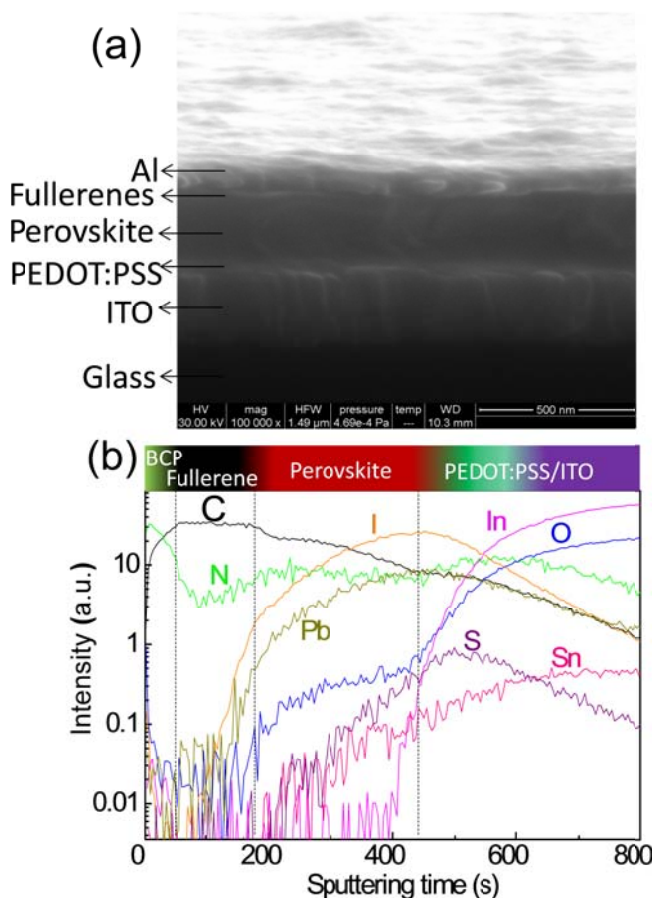


Fig. 3. (a) Cross-section SEM image of the best-performing perovskite device. The scale bar is 500 nm. The thickness of the perovskite layer is ~270 nm; (b) composition depth profiles of the device without the Al electrode measured by SIMS.

The devices have a structure of ITO/PEDOT:PSS/MAPbI₃/[6,6]-phenyl-C61-butyric

acid methyl ester (PCBM 20 nm)/C₆₀/(20 nm)/2,9-dimethyl-4,7-diphenyl-1,10-phenanthroline (BCP, 8 nm)/aluminium (Al, 100 nm). A cross-section SEM of the whole device is shown in Fig. 3a which shows a continuous, pin-hole free perovskite formed on PEDOT:PSS with film thickness variation of less than 20 nm. Secondary ion mass spectrometry (SIMS) measurement on the real device without an Al electrode, as shown in Fig. 3b, revealed a layered structure and the penetration of Pb²⁺ and I⁻ across the whole perovskite layer. The depth composition profile of Pb²⁺ and I⁻ shows a graded composition with increased Pb²⁺ and I⁻ toward the PEDOT:PSS side, which might be caused by the incomplete diffusion of traceable PbI₂ to the surface but most likely by nonuniform sputtering of the perovskite layer. Nevertheless the deficiency of Pb²⁺ on the top surface of these perovskite films was also observed by X-ray photoelectron spectroscopy measurement, as summarized in Table S2. Hall effect measurement reveal a *p*-type provskite and low extrinsic hole concentration around 4~10×10¹³ cm⁻³, which might be due to the Pb deficiency in the perovskite films formed by the interdiffusion approach in which there is excess MAI supply.²³

In our devices, a PCBM layer spun onto the perovskite layer followed by thermal annealing is used to passivate the perovskite surface and grain boundaries.²⁴ Hall effect measurements have shown that PCBM passivation can reduce extrinsic hole concentration caused by unintentional doping in solution-processed perovskite by three times and improve the carrier mobility by three times. The additional C₆₀ layer further passivates perovskite films and reduces the trap state density.²² The device performance is very sensitive to the precursor thickness ratio, thermal annealing time, and perovskite thickness. Unmatched PbI₂ or MAI thickness always results in reduced short circuit current density (*J*_{SC}) and fill factor (*FF*), which might be caused by the traceable insulating precursors or nonstoichiometric compounds.

Fig. 4a shows typical photocurrents of the devices with a fixed PbI₂ thickness (140 nm) and varied MAI thickness, demonstrating how the device performance was optimized. Fig. 4b shows the photocurrents of the devices with varied perovskite thicknesses varied from 200 nm to 320 nm. It is clear that a thicker perovskite film absorbs more light and thus yields a larger photocurrent, while a too-large thickness causes loss of photovoltage, most likely due to the increased charge recombination. The optimized MAPbI₃ devices have a perovskite thickness of 270-300

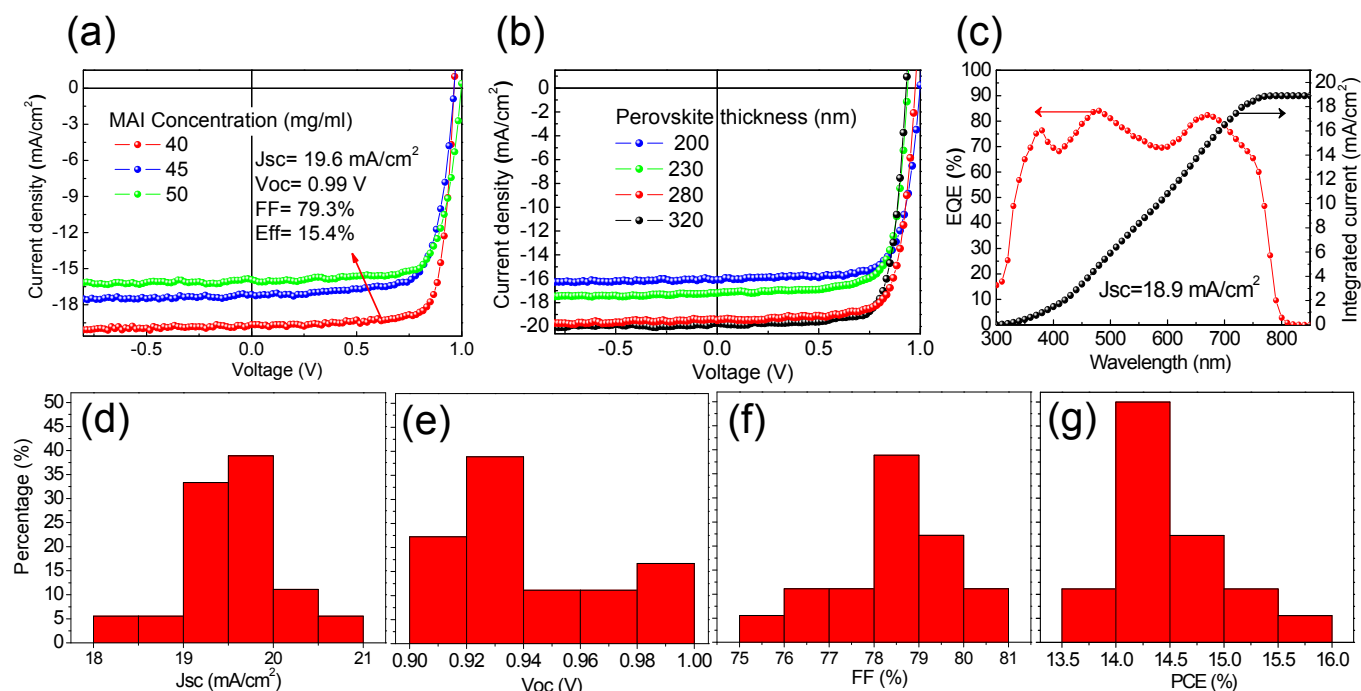


Fig. 4. Performance of the perovskite devices. (a) Photocurrents of the device with PbI_2 thickness of 140 nm while varied MAI concentration from 40–50 mg/ml; (b) Photocurrents of the devices with perovskite films of different thickness varied from 200 to 320 nm; (c) external quantum efficiency of one optimized device. (d–g) Device performance statistics based on more than 50 devices from five batches.

nm which is twofold longer than that of the previously measured low end of the electron and hole diffusion length of around 100–130 nm.^{12, 14} The long carrier extraction length should be ascribed to the excellent crystallinity, passivation by fullerenes,²⁴ and/or low extrinsic doping of perovskite films formed by interdiffusion. It demonstrates the advantages of the interdiffusion approach in the formation of high quality perovskite films. The highest PCE devices were obtained by annealing of the PbI_2/MAI with a thickness of 140/190 nm at 100 °C for 2 hours. The device was measured under AM 1.5 simulated one sun illumination.

Table I. Photovoltaic performance of a best-performing device under different illumination light intensities.

Light intensity (mW/cm ²)	J_{sc} (mA/cm ²)	V_{oc} (V)	FF (%)	PCE (%)
3.20	0.78	0.85	82.2	17.0
31	7.09	0.92	77.0	16.2
100	20.59	0.94	78.8	15.3

The device area is 9.6 mm², determined by the overlap of the cathode and anode electrodes. In order to

avoid the overestimation of the photocurrent density by the piping effect, an aperture size of 8 mm² was used to define the light absorption area.²⁵ A Schott KG5 color-filtered Si diode (Hamamatsu S1133) was used to calibrate the light intensity of the solar simulator before photocurrent measurement to avoid optical mismatch.²⁶

The best performing device has a J_{sc} of 19.6 mA/cm², FF of 79.3%, open circuit voltage (V_{oc}) of 0.99 V, and PCE of 15.4%. Fig. 4c shows the external quantum efficiency (EQE) of the device. The calculated J_{sc} from the EQE spectra is 18.9 mA/cm², which is close to the measured J_{sc} of 19.6 mA/cm². It is noted that there are two troughs in the EQE spectrum at around 400 nm and 600 nm, which is caused by the stronger reflection of the glass/ITO substrates at these wavelength regions. Another best performing device with larger photocurrent but smaller V_{oc} shows even higher efficiency of 16–17% at a lower light intensity of 3.2–30 mW/cm², as summarized in Table 1. The light intensity was tuned by applying neutral density filters of different optical densities. The higher efficiency under lower light intensity is ascribed to the reduced charge recombination evidenced by the larger FF, up to 82%. There is still room to further increase the carrier diffusion length for efficiency enhancement. Although a larger J_{sc} of 22 mA/cm² could be reached in our devices with thicker perovskite thickness, the V_{oc} and FF

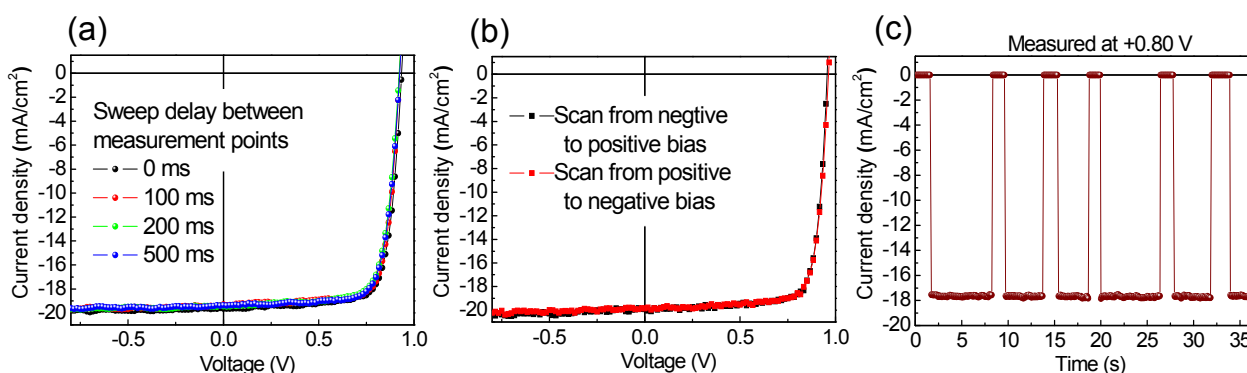


Fig. 5 (a) Photocurrents of a high performance perovskite device measured with different delays between measurement points (a) and different sweep directions (b). No obvious hysteresis of photocurrent was observed. (c) Measured photocurrent output at the maximum power point of a high performance device versus time by turning on and off the illumination with a chopper.

generally reduce, pulling down the *PCE*, which still needs a thorough understanding on the charge recombination process in perovskite materials and electrode interfaces to recover the V_{OC} and *FF*.

One significant improvement of the device performance reported in this work is from the large *FF* of around 80% for most of our devices. The statistics of *FF*, J_{SC} , and V_{OC} are shown in Fig. 4d-f. In addition to the reduced charge recombination in perovskite layers due to their good crystallinity and passivation by PCBM, both at the top surface and at the grain boundaries inside the perovskite films,²⁴ the compact and leakage-free perovskite films formed by the interdiffusion process should also contribute to the large *FF*. Most of the devices have a low saturated dark current density in the order of 10^{-4} - 10^{-3} mA/cm² at -2 V. The 15.4% device has a large shunt resistance of 4.67 k Ω -cm² and a small series resistance of 1.06 Ω -cm² calculated from the photocurrent curve which is among the best values reported. Another merit of the interdiffusion method for fabricating perovskite devices is that it gives an excellent yield of high *PCE* devices which is attractive for large-scale production of perovskite devices. The statistics of the *PCE* based on more than 50 devices from five batches are shown in Fig. 4g. The average *PCE* is 14.5% and 85% of the devices have efficiency above 14%.

It has been reported that photocurrent hysteresis appears in some perovskite devices, which is strongly dependent on the device fabrication process as well as the measurement scanning rate and directions.²⁷ The origin of photocurrent hysteresis was ascribed to either the traps, ferroelectric properties of the perovskite material and/or the electromigration of ion in the perovskites. Here we changed the scanning rate from very fast to very slow, with a delay between

measurement voltage points increased from 0 to 500 ms, which corresponds to the scan rate of 10.4 V/s to 0.033 V/s. The slowest scanning rate is comparable to what *Snaith et al.* reported.²⁷ As shown in Fig. 5a-b, no obvious hysteresis of photocurrent was observed by changing the sweep rates or direction in our devices or the sweep rates. This indicates that the origin of hysteresis in photocurrent is more likely due to the traps formation in some nonoptimized film and device fabrication process. The ultimate way to examine the efficiency of a solar cell device is to measure its power output at the load point. If there is large density of traps in the devices or photocurrent hysteresis for other reasons, the photocurrent would rise slowly upon turning on illumination. Fig. 5c shows that the photocurrent rose quickly to maximum in the timescale limited by the spin rate of the chopper, proving the presence of a negligible amount of charge traps in our optimized devices.

Conclusions

The interdiffusion method can be simply applied to other types of perovskite materials for incorporating Cl, Br, F, or other elements from precursor solutions and can also start with thermally evaporated precursor stacking layers to relieve the strict requirements for composition controlling in the co-evaporation process. The low temperature used is compatible with plastic flexible substrates. The interdiffusion approach can be potentially scaled up for large area device fabrication with established solution-process techniques, such as die-slot coating, gravure coating, and doctor blade coating.

Notes and References

¹Department of Mechanical and Materials Engineering and Nebraska Center for Materials and Nanoscience,

COMMUNICATION

University of Nebraska-Lincoln, Lincoln, Nebraska 68588-0656;

²Department of Physics and Astronomy, University of Rochester, Rochester, NY 14627;

³Institute of Super-microstructure and Ultrafast Process in Advanced Materials (ISUPAM), Central South University, Changsha, Hunan, the People Republic of China 410083

§Z.X. and C.B. contributed to this work equally.

1. J. Burschka; N. Pellet; S.-J. Moon; R. Humphry-Baker; P. Gao; M. K. Nazeeruddin; M. Grätzel, *Nature* 2013, **499**, 316.
2. M. Liu; M. B. Johnston; H. J. Snaith, *Nature* 2013, **501**, 395.
3. A. Kojima; K. Teshima; Y. Shirai; T. Miyasaka, *J. Am. Chem. Soc.* 2009, **131**, 6050.
4. M. M. Lee; J. Teuscher; T. Miyasaka; T. N. Murakami; H. J. Snaith, *Science* 2012, **338**, 643.
5. A. Abrusci; S. D. Stranks; P. Docampo; H.-L. Yip; A. K. Y. Jen; H. J. Snaith, *Nano Lett.* 2013, **13**, 3124.
6. J. M. Ball; M. M. Lee; A. Hey; H. J. Snaith, *Energ. Environ. Sci.* 2013, **6**, 1739.
7. G. Hodes, *Science* 2013, **342**, 317.
8. J. Y. Jeng; Y. F. Chiang; M. H. Lee; S. R. Peng; T. F. Guo; P. Chen; T. C. Wen, *Adv. Mater.* 2013, **25**, 3727.
9. H.-S. Kim; I. Mora-Sero; V. Gonzalez-Pedro; F. Fabregat-Santiago; E. J. Juarez-Perez; N.-G. Park; J. Bisquert, *Nat. Commun.* 2013, **4**, 2242.
10. N.-G. Park, *J. Phys. Chem. Lett.*, 2013, **4**, 2423.
11. H. J. Snaith, *The J. Phys. Chem. Lett.* 2013, **4**, 3623.
12. S. D. Stranks; G. E. Eperon; G. Grancini; C. Menelaou; M. J. Alcocer; T. Leijtens; L. M. Herz; A. Petrozza; H. J. Snaith, *Science* 2013, **342**, 341.
13. W. Zhang; M. Saliba; S. D. Stranks; Y. Sun; X. Shi; U. Wiesner; H. J. Snaith, *Nano Lett.* 2013, **13**, 4505.
14. G. Xing; N. Mathews; S. Sun; S. S. Lim; Y. M. Lam; M. Grätzel; S. Mhaisalkar; T. C. Sum, *Science* 2013, **342**, 344.
15. J. H. Heo; S. H. Im; J. H. Noh; T. N. Mandal; C.-S. Lim; J. A. Chang; Y. H. Lee; H.-j. Kim; A. Sarkar; M. K. Nazeeruddin, *Nat. Photon.* 2013, **7**, 486.
16. N.-G. Park, *J. Phys. Chem. Lett.* 2013, **4**, 2423.
17. P. Docampo; J. M. Ball; M. Darwich; G. E. Eperon; H. J. Snaith, *Nat. Commun.* 2013, **4**, 2761.
18. Tomas Leijtens; Giles E. Eperon; Sandeep Pathak; Antonio Abate; M. M. Lee; H. J. Snaith, *Nat. Commun.* 2013, **4**, 2885.
19. O. Malinkiewicz; A. Yella; Y. H. Lee; G. M. Espallargas; M. Graetzel; M. K. Nazeeruddin; H. J. Bolink, *Nat. Photon.* 2014, **8**, 128
20. G. E. Eperon; V. M. Burlakov; P. Docampo; A. Goriely; H. J. Snaith, *Adv. Funct. Mat.* 2014, **24**, 151.
21. R. F. Service, *Science* 2013, **342**, 794.
22. Q. Wang; Y. Shao, Q. Dong; Z. Xiao; Y. Yuan; J. Huang, *Energ. Environ. Sci.* 2014, Accepted.
23. W.-J. Yin; T. Shi; Y. Yan, *Appl. Phys. Lett.* 2014, **104**, 063903.
24. Y. Shao, Z. Xiao, Q. Dong, Q. Wang, C. Bi, J. Huang, **Unpublished.**
25. H. J. Snaith, *Energ. Environ. Sci.* 2012, **5**, 6513.

26. V. Shrotriya; G. Li; Y. Yao; T. Moriarty; K. Emery; Y. Yang, *Adv. Funct. Mat.* 2006, **16**, 2016.

27. H. J. Snaith; A. Abate; J. M. Ball; G. E. Eperon; T. Leijtens; N. K. Noel; S. D. Stranks; J. T.-W. Wang; K. Wojciechowski; W. Zhang, *J. Phys. Chem. Lett.* 2014, **5**, 1511